Journal of the Meteorological Society of Japan, Vol. 84, No. 1, pp. 165–185, 2006

20-km-Mesh Global Climate Simulations Using JMA-GSM Model —Mean Climate States—

Ryo MIZUTA, Kazuyoshi OOUCHI

Advanced Earth Science and Technology Organization, MRI, Tsukuba, Japan

Hiromasa YOSHIMURA, Akira NODA

Meteorological Research Institute, Tsukuba, Japan

Keiichi KATAYAMA

Japan Meteorological Agency, Tokyo, Japan

Seiji YUKIMOTO, Masahiro HOSAKA, Shoji KUSUNOKI

Meteorological Research Institute, Tsukuba, Japan

Hideaki KAWAI and Masayuki NAKAGAWA

Japan Meteorological Agency, Tokyo, Japan

(Manuscript received 20 April 2005, in final form 28 October 2005)

Abstract

A global atmospheric general circulation model, with the horizontal grid size of about 20 km, has been developed, making use of the Earth Simulator, the fastest computer available at present for meteorological applications. We examine the model's performance of simulating the present-day climate from small scale through global scale by time integrations of over 10 years, using a climatological sea surface temperature.

Global distributions of the seasonal mean precipitation, surface air temperature, geopotential height, zonal-mean wind and zonal-mean temperature agree well with the observations, except for an excessive amount of global precipitation, and warm bias in the tropical upper troposphere. This model improves the representation of regional-scale phenomena and local climate, by increasing horizontal resolution due to better representation of topographical effects and physical processes, with keeping the quality of representation of global climate. The model thus enables us to study global characteristics of small-scale phenomena and extreme events in unprecedented detail.

Corresponding author: Ryo Mizuta, Advanced Earth Science and Technology Organization, Meteorological Research Institute, 1-1 Nagamine, Tsukuba, Ibaraki 305-0052, Japan.
E-mail: rmizuta@mri-jma.go.jp

1. Introduction

To evaluate the possible affect of global warming upon the meteorological phenomena of small scales in time and space is important, not only from the scientific, but also from the socio-economic viewpoints. As concentrations of greenhouse gases increase in the atmosphere, the Intergovernmental Panel on Climate Change (IPCC) report (IPCC 2001) projected increase of surface air temperature, more hot days, and fewer cold days and frost days over nearly all land areas. Diurnal temperature range is projected to decrease. Heavy precipitation possibly increases, due to water vapor increase in the atmosphere. While possible changes of extreme events induced by the global warming was described in the IPCC report, the description remained qualitative, partly due to the limited resolution of the existing climate models. Even the directions of the projected changes were almost uncertain for some kinds of the extreme events. By the recent advances in the computational environment, however, we have become able to run a climate model, with resolution high enough to investigate global characteristics of small-scale phenomena, and extreme events in detail.

We have developed a 20-km-mesh super high-resolution global atmospheric general circulation model on the Earth Simulator (ES). The ES is a parallel-vector supercomputer system, consisting of 5120 processors (Habata et al. 2004), which was ranked as the fastest computer in the world when our calculations were carried out. Our goal is to obtain scientific insights into the possible affects of global warming on small-scale phenomena, such as tropical cyclones and Baiu fronts in the East Asian summer monsoon, with this high resolution global atmospheric climate model. The model is developed to enable us to simulate a realistic climate with high accuracy, through the improvements for calculation schemes and physical processes.

So far, no existing global climate models, that stand long time integration, conserve mass, and simulate realistic global climate, have used resolution as fine as 20-km mesh. The 10-km-mesh model, the highest resolution of global atmospheric models, has succeeded in simulating tropical cyclones, extratropical cyclones with fronts as the initial value problem (Ohfuchi et al. 2004), but its integration period was limited to a couple of weeks. Short-term integrations of global models with even higher resolution are tried by several groups. As long-term climate simulations, Duffy et al. (2003) performed an 11-year simulation with T239L18 (50-km mesh), using National Center for Atmospheric Research (NCAR) CCM3 model. Ohfuchi et al. (2004) also conducted a 12-year simulation with T319L24 (40-km mesh). With the increase of horizontal resolution up to 20-km mesh, the model becomes able to represent interactions among the phenomena of meso-beta scale and synoptic or planetary scale more explicitly than other existing models. The phenomena in which the multi-scales disturbances play important roles, such as developments of tropical cyclones or Baiu fronts, become possible to see in detail in the climate simulation. Taking constraints of computational resources into consideration, we chose the resolution in order that we can perform long-term integrations within a reasonable calculation time. As for technical aspects, we expect that we can apply the same parameterizations as the coarser-resolution models to the 20-km-mesh global model without substantial modification, since similar parameterizations have already been used in a 20-km-mesh regional model.

Regional climate models have been conventionally used for climate simulations with high horizontal resolutions up to 20-km mesh, where lateral boundary conditions are nested from either global atmospheric models or atmosphere-ocean coupled models. Compared with these regional models, the high-resolution global model has advantages that it can avoid problems with the lateral boundary condition, and that it can incorporate interactions between global scale and regional scale explicitly. Moreover, as a matter of course, the global model gives information on regions that regional models have not covered.

A present-day climate simulation was performed over 10 years, using the 20-km-mesh model with the ES, by prescribing an observed climatological sea surface temperature (SST) as a lower boundary condition. In this paper, we describe the model's performance of simulating the present-day climate.

As we use a higher resolution model than before, smaller-scale phenomena is represented explicitly. Such phenomena can interact with larger-scale phenomena and can influence global-scale features. Before investigating simulated small-scale phenomena, and impacts of global climate change on them, it is necessary to examine whether the model can realistically simulate global-scale, long-term mean climate state as well. In this paper, we present the model's performance of representing global-scale, long-term mean climate state, and representing regional-scale climate state in some aspects. Several lower-resolution simulations, with the same model framework, are also conducted to compare the results with those from the high-resolution model to examine resolution dependence. Details about the simulated small-scale phenomena and extreme events, such as tropical cyclones and Baiu front, are reported in separate publications.

Descriptions of the model, and the developments for the 20-km-mesh model are in the next section. The design of the experiments is in Section 3. The model's performance of representing present-day climate state is discussed in Section 4, and concluding remarks are presented in Section 5.

2. Model developments

2.1 Model outline

The model used in this study is a prototype of the next generation of global atmospheric model of the Japan Meteorological Agency (JMA). Meteorological Research Institute (MRI), and JMA are in collaboration to develop the model for the use of both climate simulations and weather predictions. The model is based on the global numerical weather prediction (NWP) model of JMA (JMA-GSM0103), upon which modifications and improvements have been implemented.

Since detailed description of the JMA-GSM0103 model is available in JMA (2002), we give only an outline here. The dynamical framework is a full primitive equation system, originally designed by Kanamitsu et al. (1983). It uses a spectral transform method of spherical harmonics, and a sigma-pressure hybrid coordinate as the vertical coordinate. The cumulus convection scheme proposed by Arakawa and Schubert (1974) is implemented. The vertical profile of the upward mass flux is assumed to be a linear function of height, as proposed by Moorthi and Suarez (1992). The mass flux at the cloud base is determined by solving a prognostic equation (Randall and Pan 1993; Pan and Randall 1998). Clouds are prognostically determined in a similar fashion to that of Smith (1990), in which the cloud amount and the cloud water content are estimated by a simple statistical approach proposed by Sommeria and Deardorff (1977). The phase of cloud is assumed liquid above 0°C and ice below −15°C, and the fraction of each changes linearly with temperature between −15°C and 0°C. The parameterization of the conversion rate from cloud water to precipitation follows the scheme proposed by Sundqvist (1978). The level 2 turbulence closure scheme by Mellor and Yamada (1974) is used to represent the vertical diffusion of momentum, heat and moisture. The orographic gravity wave drag scheme developed by Iwasaki et al. (1989) is used, in which gravity waves are partitioned into long waves (wavelength $>$ 100 km) and short waves (wavelength $\sim$ 10 km). The long waves propagate upward and deposit momentum in the middle atmosphere, while the short waves are trapped in the troposphere and exert drag there.

2.2 Developments implemented on the model

Modifications described below have been implemented on JMA-GSM0103 to build the model in this study.

First, a new quasi-conservative semi-Lagrangian scheme (Yoshimura and Matsumura 2003) has been developed and introduced for stable and efficient time integrations. Horizontal and vertical advections are calculated separately in this scheme. The vertical flux is determined with rigorous conservation in a conservative semi-Lagrangian scheme. The horizontal advection is calculated in a standard semi-Lagrangian scheme, but mass, water vapor, and cloud water are conserved using a correction method similar to Priestley (1993) and Gravel and Staniforth (1994). Prognostic variables have been changed from vorticity and divergence, to zonal and meridional wind components with the introduction of the semi-Lagrangian scheme (Ritchie et al. 1995). Since time steps are not constrained by the CFL criterion when the semi-Lagrangian scheme is used, we can use much longer time steps in the scheme than in a conventional Eulerian scheme. Furthermore, a two-time-level semi-Lagrangian scheme has been introduced instead of a three-time-level scheme, which provides a doubling of efficiency in principle (Temperton et al. 2001; Hortal 2002; Yoshimura and Matsumura 2005). These improvements of efficiency enable us to perform high-resolution, long-term integrations.

Second, some physical process schemes have been improved. A cumulus parameterization scheme has been improved to include the entrainment and detrainment effects between the cloud top and cloud base in convective downdraft instead of reevapolation of convective precipitation (Nakagawa and Shimpo 2004). This reduces cooling bias in the tropical lower troposphere of the model, as cooling by the reevapolation is reduced. The cloud ice fall scheme, based on an analytically integrated solution by Rotstayn (1997), has been introduced (Kawai 2003), instead of a rather simple parameterization in which cloud ice falls only into the next layer, or to the ground. The prognostic cloud scheme has been modified to reduce the dependence of precipitation on the integration time step. In order to represent subtropical marine stratocumulus off the west coasts of the continents, a new stratocumulus parameterization scheme has been introduced, following a simple and classical one proposed by Slingo (1987), with some modifications (Kawai 2004). Cloud is formed in the model when there is inversion at the top of boundary layer, and mixing layer is formed near the sea surface.

2.3 *Schemes and settings for a climate model*

The radiation scheme and the land surface scheme, developed for a climate model MRI/JMA98 GCM (Shibata et al. 1999), has been introduced to the model with some modifications. We use these detailed schemes, instead of the simplified but fast original schemes developed for the use of NWP.

A multi-parameter random model, based on Shibata and Aoki (1989), is used for terrestrial radiation. Absorption due to CH_4 and N_2O is treated in the present version, in addition to H_2O, CO_2, and O_3. The model calculates solar radiation formulated by Shibata and Uchiyama (1992), with delta-two-stream approximation. An explicit treatment of the direct effect of sulfate aerosols is considered in the present scheme.

The treatment of land surface has been improved from the Simple Biosphere model (Sellers et al. 1986), mainly in the soil and snow schemes. In the soil scheme, the 3 layers for the soil water equation are shared with the heat budget equation, and the phase changes of water are included, so that the water and energy can be conserved in the soil layers. It also has the 4th layer as a heat buffer. In the snow scheme, the number of snow layers varies up to 3, depending on the snow amount, and the heat and water fluxes are calculated. Snow albedo depends on the snow age (Aoki et al. 2003).

The simulations were performed at a triangular truncation 959, with the linear Gaussian grid (TL959) in the horizontal, in which the transform grid uses 1920×960 grid cells, corresponding to the grid size of about 20 km. The linear Gaussian grid has a smaller number of grid points than the ordinary 'quadratic' Gaussian grid, for the same spectral resolution. We can use the linear grid, because quadratic Eulerian advection terms which bring about aliasing do not appear in the semi-Lagrangian scheme. Details about the linear Gaussian grid can be found in Hortal (2002) and the references therein. The model uses 60 levels in the vertical, with the model top at 0.1 hPa. If we use an Eulerian scheme of the same horizontal resolution, we need a time step less than about 1 minute to satisfy the CFL criterion. But the time step we use in this study is 6 minutes, since it is not constrained by the criterion when we use a semi-Lagrangian scheme. The time step of 6 minutes is chosen in consideration of computational instabilities unrelated to the CFL criterion.

2.4 *Physical parameterizations*

Originally, all the settings in the physical parameterizations were 'tuned' at the resolutions of 300 to 60 km. When the settings were applied to the 20-km-mesh resolution without any modification, many problems arose from characteristics depending on resolution. For instance, 1) the amount of global average precipitation increased, 2) the temperature at tropical upper troposphere became higher, and 3) cloud amount decreased as the horizontal resolution got higher. In addition to these resolution dependences, resolution independent characteristics of the model, which did not need to be considered at lower resolutions, became conspicuous; convection was obviously less organized in meso-beta scale than observation, and frequency of tropical cyclones generation was less than observation. Therefore, some parameterizations of sub-grid scale physical processes were adjusted in order to reduce these biases. We tried several sets of the adjustments described below, but we could not do systematic parameter sweep experiments, due to constraint of computation resources and the time schedule.

Inhomogeneity of field variables (e.g., temperature, wind speed, etc.) of the model in a certain large (say, 300 km) fixed domain would increase with higher resolution, even though the area-mean values do not change. Evaporation therefore increases, since it is a function of the square of wind speed. So we make 10% less estimation of evaporation in the TL959 model than in the other resolution models. The amount of precipitation, however, is not changed so much, since negative feedback works against the modification.

On the other hand, a deviation from the grid-mean value, which cannot be resolved by the model would become smaller as the resolution becomes finer. Therefore, assumed sub-grid variance of water vapor is set to be 10% smaller in the cloud scheme of the TL959 model. This modification decreases the over-estimated condensation, and prevents instability from dissolving too fast, resulting in promoting organization of convection. This is effective also in decreasing the resolution dependence of global average precipitation.

We decreased the amount of detrainment of cloud water at the top of the cumulus convection, as well as transformation speed from cloud water to precipitation in the cloud scheme. These are implemented in order that cumulus and layer cloud increase, and resolution dependence decreases. These are also effective in decreasing the amount of global average precipitation. Values of parameters are selected so that the radiation balance is consistent with observations.

Among a number of modifications implemented in the physical processes of the TL959 model, the most effective one for improving the representation of tropical cyclones is to decrease the vertical transport of horizontal momentum in the convection scheme. The ensemble effect of the convective momentum transport is generally downgradient, and acts to reduce the vertical wind shear of tropical cyclones. When a convective-scale pressure gradient force (Wu and Yanai 1993; Gregory et al. 1999) is not included in the convection scheme, the downgradient momentum transport is overestimated, which weakens tropical cyclones excessively. Therefore, as a simple approximation of the effect of the pressure gradient force, we reduce the estimation of the effect of the momentum transport by 60%, resulting in more realistic organization of tropical cyclones.

We set the surface roughness length over the ocean to be larger, in order to enhance thermal interaction between sea surface and boundary layer. This also improves the representation of tropical cyclones. We set gravity wave drag coefficient for short waves, to be increased in order to control excessive developments of extratropical cyclones. As for the time step, because of the introduction of a semi-Lagrangian scheme, the time step used in the TL959 is not shorter than the one used in a coarser-resolution version with a Eulerian scheme. Therefore, effects by the time step on the physical parameterizations are not so crucial in the TL959.

2.5 Computational environments

The model development and calculations have been carried out on the ES. The ES is a distributed memory parallel computer system, which consists of 640 processor nodes. Each processor node is a shared memory system, which contains 8 vector processors. We have optimized the model codes for the ES. The Message Passing Interface (MPI) library is used for inter-node parallelization, and microtasking, which is shared memory parallel programming, is used for intra-node parallelization. The computing efficiency is better than 30% of the peak performance. It takes about 4 hours to execute one-month integration of the TL959L60 model using 30 nodes (240 CPUs) of the ES.

3. Experimental design

Time integration over 10 years was carried out with the resolution of TL959L60 as a present-day climate simulation of the global atmospheric model. Its performance of representing climate is examined by the result. As boundary conditions, we used the monthly mean climatological sea surface temperature (SST), and sea ice concentration by Reynolds and Smith (1994), averaged from November 1981 to December 1993. The SST is updated daily using linear interpolation from the monthly climatology. Concentrations of the greenhouse gases are set constant at 348 ppmv for CO_2, 1.650 ppmv for CH_4, and 0.306 ppmv for N_2O. Climatological monthly mean three-dimensional distributions of sulfate aerosols, calculated on the global chemical transport model by MRI (Tanaka et al. 2003), are incorporated into the model.

The initial condition is provided by a global objective analysis of the JMA at July 9, 2002. After a spin-up with slight parameter change for 5 and a half years, the integration for 10 years was conducted. Although no interannual variation of the external forcing (i.e., SST, greenhouse gases, etc.) is imposed in the experiment, there exists interannual variability, caused by internal variability of the atmosphere. We discuss here the time mean climate state averaged over the 10 years. We use SST without interannual variability as a boundary condition, because this calculation is used as a control run against a time-slice experiment of future climate, in which SST difference, between present-day and warmed climate atmosphere-ocean coupled GCM, is added to the SST given here.

To examine resolution dependence of the results, we also performed simulations with three lower spatial resolutions, using the same model frame-work. The resolutions are TL63L40 (128×64 grid cells and 40 vertical levels up to 0.4 hPa, about 270 km grid size), TL95L40 (192×96, 180 km) and TL159L40 (320×160, 110 km). In these additional simulations, the parameter adjustments described in Section 2 were not included, except for the modification on vertical transport of horizontal momentum. The time steps are 30 minutes in all three resolutions.

4. Results

This section demonstrates fundamental model performance of reproducing global-scale climatologies of precipitation, global-mean energy budgets, zonal-mean temperature and wind, geopotential height, surface air temperature, and storm track activity. Subsequently, simulated regional-scale climate phenomena will be shown for typical concerns, Asian summer monsoon, wintertime precipitation distribution in Japan, and snow cover in Europe. A more complete set of large-scale climatologies, and their comparisons with observational estimates will be available on our website (http://www.mri-jma.go.jp/Project/RR2002/k4-1-en.html).

4.1 Precipitation

Geographical distributions of precipitation of the 10-year mean integration during boreal winter (December, January, and February), and summer (June, July, August) are shown in Figs. 1a and 2a, respectively. Their zonal means are shown on the right side (Figs. 1b and 2b), compared with data sets from observation (CMAP: Xie and Arkin 1997; and GPCP: Huffman et al. 1997). Geographical distributions of CMAP (Figs. 1c and 2c), and differences between the model and CMAP (Figs. 1d and 2d), are also presented. The results agree well with the observations in terms of spatial patterns, such as ITCZ, SPCZ, Asian summer monsoon, and storm tracks in the north Pacific and the north Atlantic in winter. Quantitatively, around the tropics of JJA, the amount is under-estimated in the western Pacific region, and over-estimated around the Bay of Bengal, the eastern Pacific and the Atlantic.

We can see precipitation patterns associated with topography. Contrast in the amount of precipitation between both sides of mountains is well simulated in New Zealand, Tasmania, south of the Andes of JJA, and in the west coast of North America and Scandinavia in DJF, which are located at the end of storm tracks. A more detailed pattern in Asian summer is also simulated, and will be presented later.

Zonal mean in both seasons (Figs. 1b and 2b) in the midlatitudes is close to that of GPCP, while that in lower latitudes is close to that of CMAP. The amount of precipitation in the tropics are over-estimated, both in winter and summer, resulting in overestimation of the global amount. The annual mean global amount of precipitation (3.06 mm/day) is about 15% larger than the estimations from GPCP (2.62 mm/day) and CMAP (2.68 mm/day).

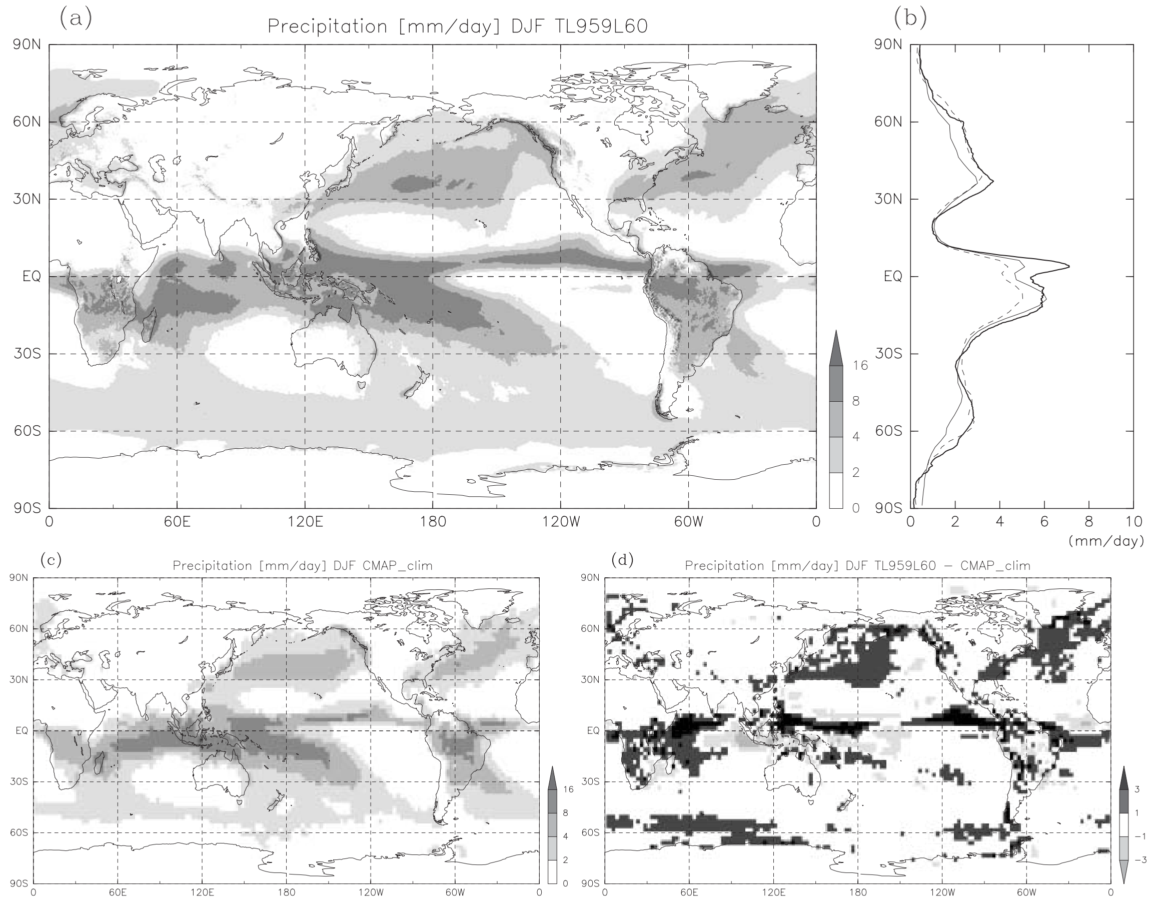

Fig. 1. Horizontal distribution of 10-year-average precipitation in DJF for (a) the TL959 model, (c) climatological estimates of CMAP and (d) difference between the TL959 model and CMAP. The difference is calculated on the grid cells of CMAP ($2.5° \times 2.5°$) by averaging the model results on the cells. (b) is the zonal mean precipitation of the model (thick solid line), CMAP (thin solid line) and GPCP (thin dashed line). Units are mm/day.

Figure 3 shows dependence of annual mean precipitation on the model resolutions, global average, average over tropics, and average in middle and high latitudes. Comparing the result of TL959L60 with TL63L40 (about 270-km mesh) and TL159L40 (about 110-km mesh) models, the global average of precipitation increases with the resolution. As the resolution increases, the amount of convective precipitation decreases and that of grid-scale precipitation increases. Note that parameter adjustments are added in the TL959 model, resulting in reduction of the increase of precipitation. Comparing the models of TL63, TL95 and TL159, in which the same parameter sets are used, a systematic tendency is found that the average in the tropics increases with resolution, while any remarkable dependence on the horizontal resolution is not seen in the extratropics.

As the resolution increases, vertical velocity is much more resolved horizontally, and amplitude of vertical velocity becomes larger, since the size of each grid cell becomes smaller. Spatial structure of humidity is also resolved more clearly, and water vapor become easily saturated in a small grid cell than in a large one. Therefore precipitation due to grid-scale condensation increases. Precipitation due to convective parameterization scheme is expected to

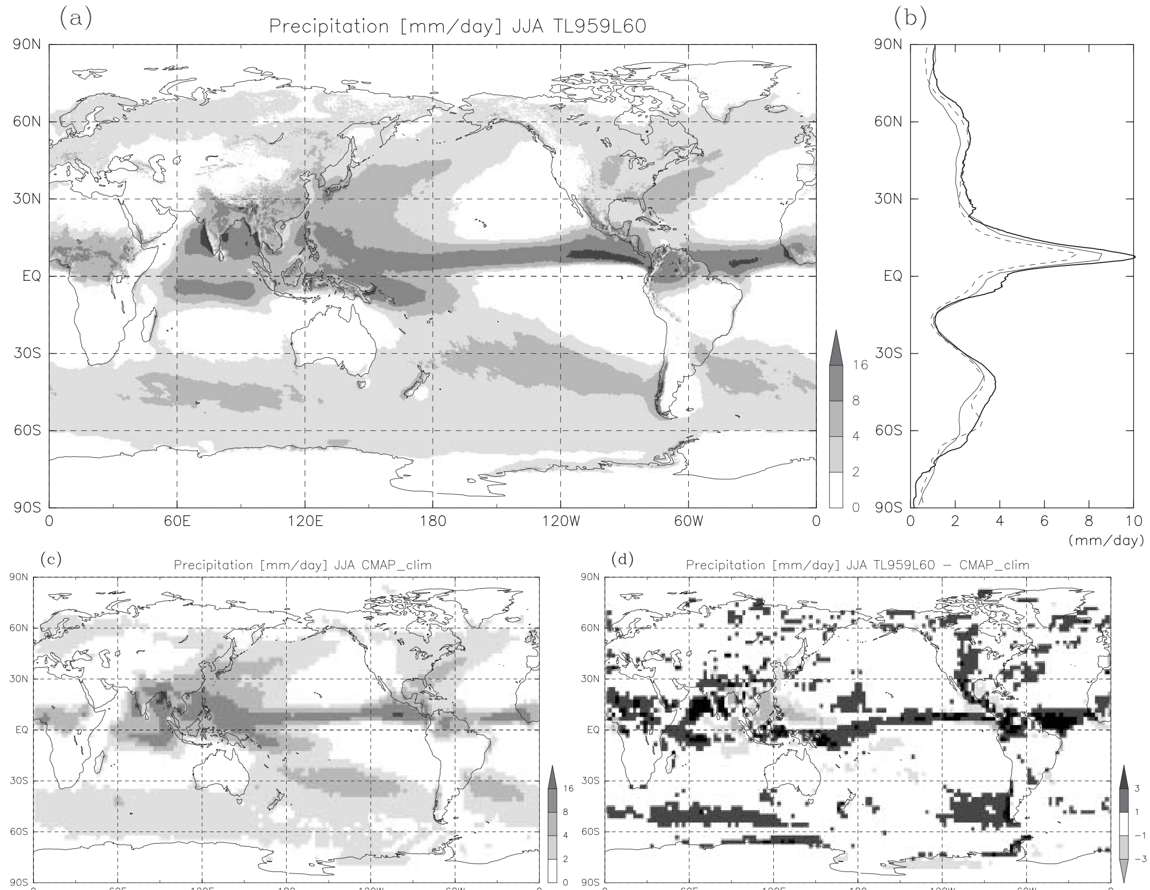

Fig. 2. As Fig. 1, but in JJA.

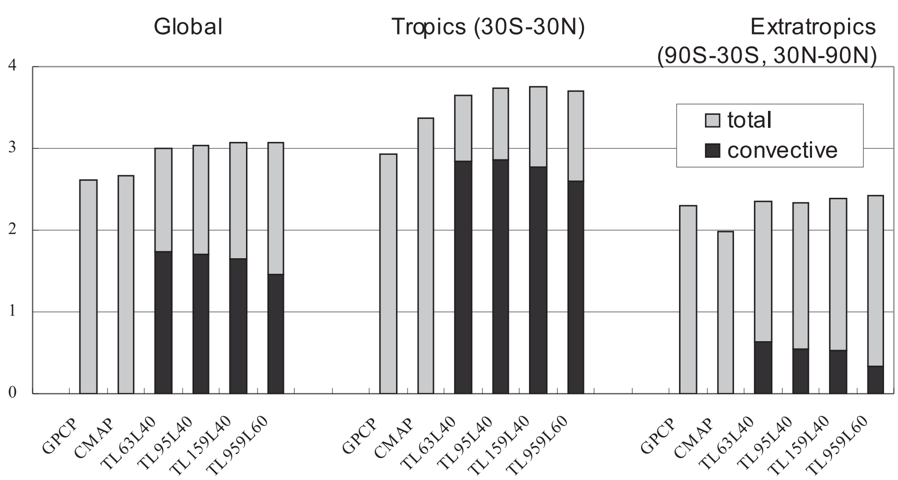

Fig. 3. Annual mean precipitation for 10-year-average for various resolutions of the model, compared with climatological estimates of GPCP and CMAP. Units are mm/day. For the models, dark shaded is convective precipitation, and light shaded is large-scale precipitation. (left) global average, (center) average in the tropics (30 S–30 N), and (right) average in the extratropics (90 S–30 S, 30 N–90 N).

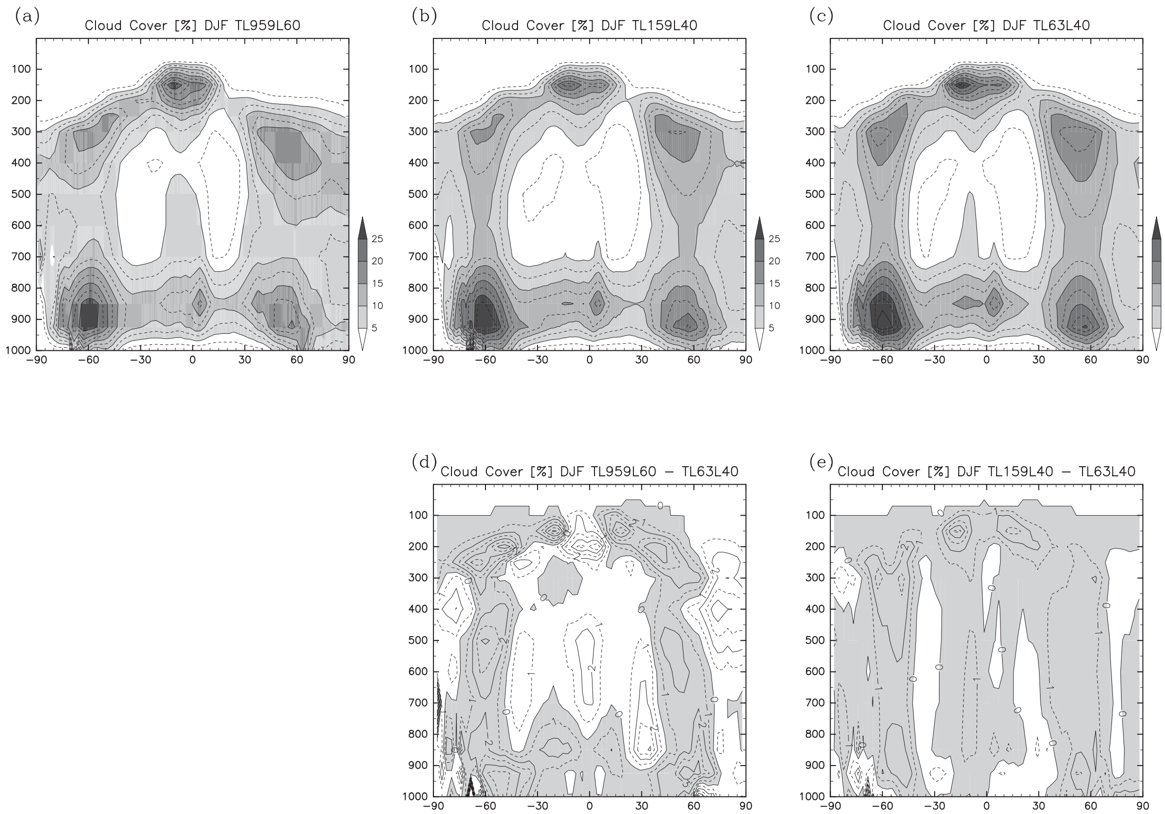

Fig. 4. Seasonal averages of zonal-mean cloud cover in units of % in DJF for (a) the TL959 model, (b) the TL159 model, and (c) the TL63 model. (d) is difference between the TL959 and the TL63 models, and (e) is difference between the TL159 and the TL63 models. Negative values are shaded in (d) and (e). Contour intervals are 2.5% in (a–c), and 1% in (d, e).

decrease, and the amount of decrease is expected to be equal to the amount of increase of grid-scale precipitation. In our results, the increase of grid-scale precipitation is slightly greater than the decrease of convective precipitation. Consequently, the total amount increases with higher resolution. The resolution dependence that the precipitation amount due to grid-scale condensation increases with more-resolved vertical velocity is consistent with those of many resolution dependence studies with atmospheric general circulation models (Williamson et al. 1995; Stratton 1999; Brankovic and Gregory 2001; Duffy et al. 2003; Kobayashi and Sugi 2004).

4.2 Cloud cover

Figure 4 shows seasonal averages of zonal-mean cloud cover in DJF simulated in the models of TL959, TL159 and TL63 resolutions. As the resolution increases, cloud cover generally decreases. Note that some increase is seen in the tropics of middle-upper troposphere in the TL959 model (Fig. 4d), since many adjustments for the high-resolution model is included. The pattern of the difference between the TL159 model and the TL63 model (Fig. 4e) is a typical one of the resolution dependence in this model, and it was emphasized in the TL959 model without any adjustment (not shown). Decreases in the upper troposphere and lower troposphere are larger than in the other regions. Cloud cover in the extratropics from 50°N to 60°N, and from 50°S to 60°S in the middle troposphere also decreases.

Kiehl and Williamson (1991) examined the dependence of the cloud fraction on horizontal resolution, using their atmospheric climate

Table 1. Global annual mean quantities related to the energy budget for 10 years of the models compared with observations or best estimates by Kiehl and Trenberth (1997). Units are W/m^2.

Quantity	TL63L40	TL159L40	TL959L60	Observations
Outgoing shortwave at TOA	109.8	108.6	109.2	107
Outgoing longwave at TOA	233.3	234.6	235.1	235
Net outgoing budget at TOA	1.0	0.9	2.2	0
Clear-sky outgoing shortwave at TOA	47.3	47.4	48.8	56
Clear-sky outgoing longwave at TOA	264.0	265.3	265.9	264
Net absorbed shortwave at surface	165.9	167.0	164.7	168
Net outgoing longwave at surface	61.5	61.1	60.7	66
Sensible heat flux	19.0	18.8	19.3	24
Latent heat flux	85.9	88.2	87.8	78
Net outgoing budget at surface	0.6	1.1	3.0	0

model, and found a systematic decrease of cloud amount when the resolution increases from R15 ($\sim 4.5^\circ \times 7.5^\circ$) to T106 ($\sim 1.1^\circ \times 1.1^\circ$). Decreases in the lower troposphere in the tropics and in the lower and upper troposphere in the extratropics are apparent in their results. They argue that the decrease of cloud in the lower atmosphere is due to increased advective drying by stronger subsidence, which results from stronger upward motion in the convective region. Decrease in the lower level ($\sim$ 800 hPa) in Figs. 4d and 4e is consistent with that examination, and as on increase of precipitation, a similar tendency is reported in other studies on resolution dependence (Phillips et al. 1995; Williamson et al. 1995; Pope and Stratton 2002). The dependence of cloud cover in the upper level and the extratropics seems to depend on the physics embedded in the model. It was attributed to a correction factor to eliminate negative moisture in Kiehl and Williamson (1991), and to a tuning parameter for radiative balance in Pope and Stratton (2002). In our model, it is reported that the amount of cloud ice fall become excessive as the time step becomes smaller (Kawai 2005). The change of cloud ice fall causes a large part of the dependence of cloud cover in the upper level and the extratropics in our model, as shown in Fig. 4d.

4.3 *Energy budget*

Table 1 shows global annual-mean quantities related to the energy budget for three resolutions of the model. The observed values listed on the table are taken from Kiehl and Trenberth (1997). Zonal-mean outgoing longwave and shortwave radiations at the top of atmosphere in January and July in the TL959 model and the TL63 model are shown in Fig. 5, which are compared with the plots from satellite measurements, between 1985 and 1988 by ERBE (Harrison et al. 1990). Note that the global-mean longwave radiation in the TL959 model has been reduced to agree with the observation through the parameter adjustment described in Section 2. As a result of the adjustment, outgoing longwave radiation agree with the observation also in the zonal-mean distribution (Figs. 5a and 5b). The global mean of outgoing shortwave at the top of the atmosphere is slightly larger than the observation (Table 1). Overestimation of the shortwave flux is found in the low latitudes (Figs. 5c and 5d), associated with overestimation of clouds around the western Pacific and the Indian Ocean. On the other hand, the global mean of clear-sky outgoing shortwave is smaller than the observation for any horizontal resolutions. It is attributed to a contribution from the ocean, especially in the summer hemisphere. Settings of the ocean surface albedo, and underestimation of scattering by aerosols, may have caused the difference.

As for the resolution dependence, Figs. 5a, 5b and Table 1 indicate that outgoing longwave radiation at the top of the atmosphere increases as resolution increases. This is consistent with the decrease of cloud cover in the upper troposphere, as the decrease of upper cloud makes the lower atmosphere exposed more

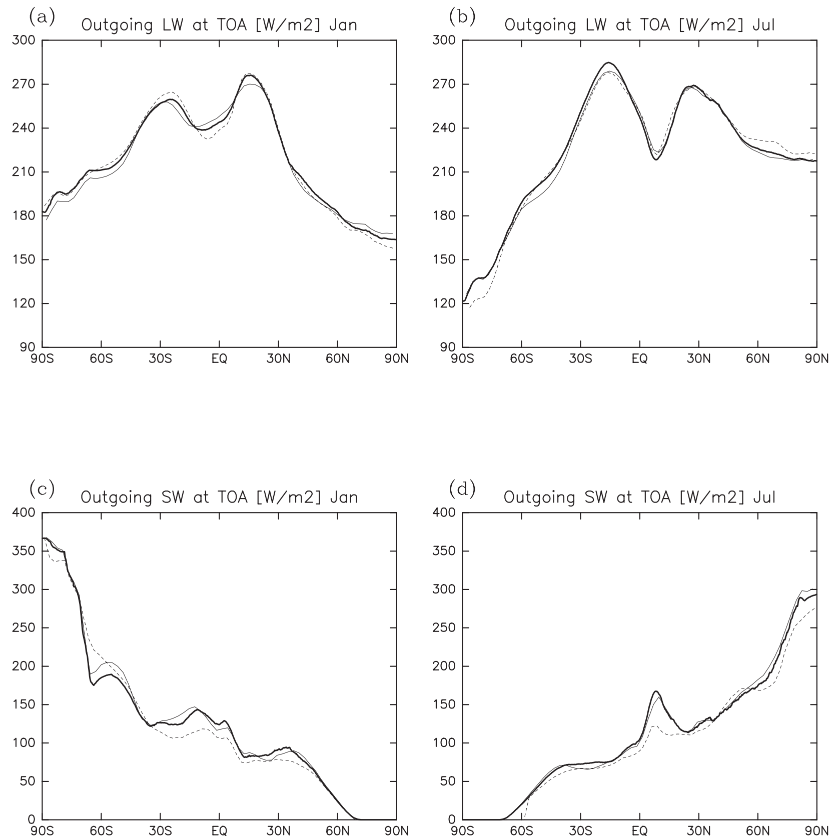

Fig. 5. Monthly averages of zonal-mean outgoing longwave (a, b) and shortwave (c, d) radiation in January (a, c) and July (b, d). Thick solid lines are the TL959 model results, and thin solid lines are the TL63 model results. Dashed lines indicate those from satellite measurements from 1985 to 1988 by ERBE.

to the space. Latent heat flux also increases, associated with the increase of precipitation resulting from an enhanced hydrological cycle.

4.4 Zonal-mean wind and temperature

Seasonal averages of zonal-mean zonal wind velocities of the model are shown in Figs. 6a and 6d. Compared with ERA40 (Simmons and Gibson 2000) reanalysis data (Figs. 6b and 6e), differences of zonal winds are within 2 m/s in most region of the troposphere, and 95% significant difference is seen only in the polar region in the southern hemisphere, and the stratosphere. Figures 6c and 6f are the difference between the results for the TL63 model and the reanalysis data. We can see difference from ERA40 is obviously decreased as resolution increases. Note that the differences with barotropic structure seen in Figs. 6c and 6f are not significant, due to large interannual variability, and can be reduced to some extent by changing the gravity wave drag coefficient (not shown).

Figures 7a and 7d show seasonal averages of zonal-mean temperatures. Although differences from ERA40 (Figs. 7b and 7e) are within 2 K in large part of the troposphere, temperature in the lower troposphere below 700 hPa is lower, and that above 700 hPa is higher than the reanalysis data in both seasons. The difference is large and significant in the tropics of the upper troposphere. Compared with the difference between the TL63 model and the reanalysis data (Figs. 7c and 7f), temperature in the middle and upper troposphere gets higher as resolution increases. This results from enhanced condensation heating associated with enhanced

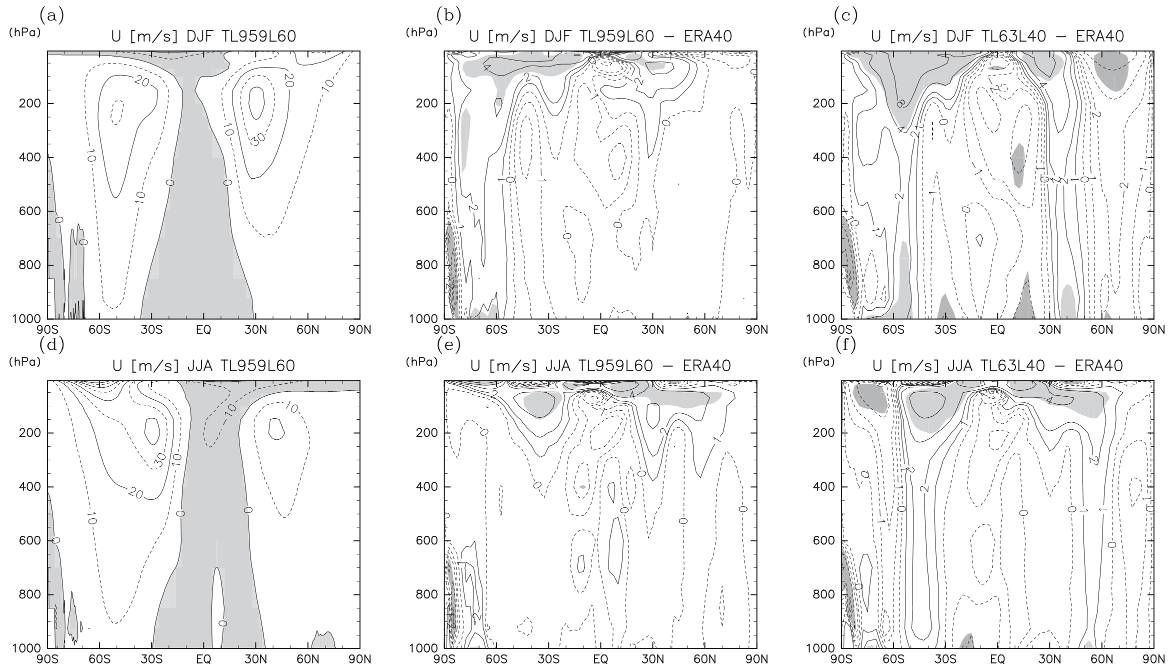

Fig. 6. Seasonal averages of zonal-mean zonal wind in DJF (top) and JJA (bottom). (a, d) are results for the TL959 model, (b, e) are differences between the TL959 model and ERA40 climate (averaged from 1979 to 2001), and (c, f) are differences between the TL63 model and ERA40. Units are m/s. Contour intervals are 10 m/s in (a, d), and 1 m/s in the others. Negative values are shaded in (a, d), and the areas where the difference is 95% significant are shaded in (b, c, e, f).

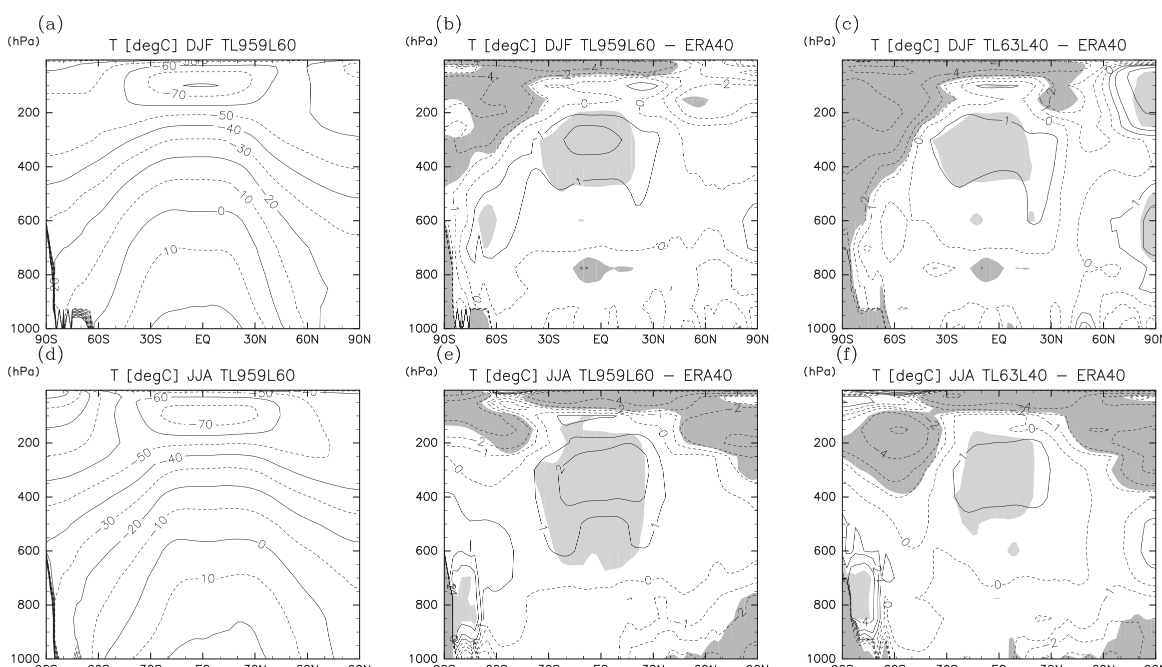

Fig. 7. As Fig. 6, but for zonal-mean temperature in °C. Contour intervals are 10 K in (a, d), and 1 K in the others. The areas where the difference is 95% significant are shaded in (b, c, e, f).

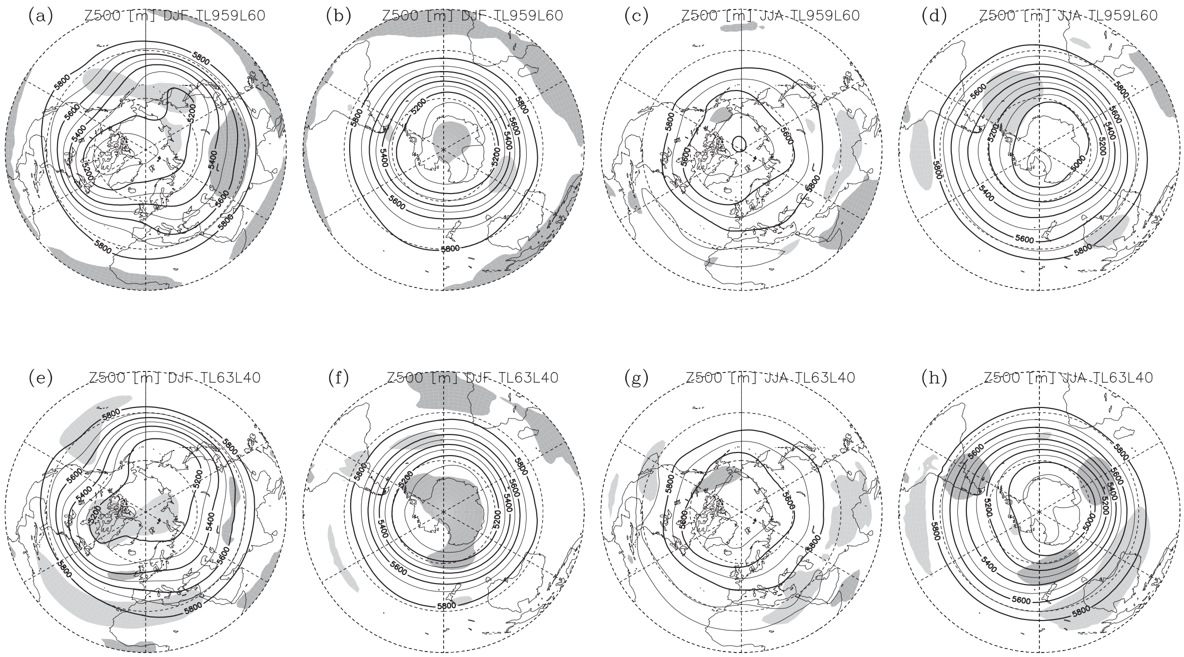

Fig. 8. Seasonal averages of 500 hPa height in meter units in DJF (left) and JJA (right) for the TL959 model (top) and the TL63 model (bottom). (a, c, e, g) are for the northern hemisphere, and (b, d, f, h) are for the southern hemisphere. Contour intervals are 100 m. The areas where the difference from ERA40 reanalysis data is 95% significant are shaded (light-shaded region for positive difference and heavy-shaded for negative difference).

latent heat transport, and enhanced precipitation in the tropics as shown in Figs. 1, 2 and Table 1.

Temperature in the lower and middle stratosphere is lower than the ERA40 climate. Since the stratosphere involves large interannual variabilities, it is necessary to perform many years of integration for comparing with the observational climatology. For that reason, the stratosphere were left "untuned" in the present version of the model. Resolution dependence of the stratospheric temperature is smaller than the difference from the analysis.

4.5 Z500

Figure 8 shows seasonal average of geopotential height at 500 hPa, for the TL959 and the TL63 models, in the northern and southern hemisphere, in DJF and JJA. The areas where the difference from ERA40 reanalysis data is 95% significant are shaded. It seems that distinct improvement with increasing resolution does not exist for the results in this aspect. Difference from the reanalysis data decreases around the North Atlantic, Greenland and Antarctic in DJF, and south of Australia in JJA. On the other hand, difference increases near the equator, associated with the temperature bias in Fig. 7.

4.6 Surface air temperature

Surface air temperature in the model is defined as air temperature 2 m above the surface, which is extrapolated from the vertical temperature profile of the lowest layers. Figure 9 shows the mean surface air temperature of the simulation in January, April, July, and October, respectively. Improvements on aged snow albedo, implemented into the model following Aoki et al. (2003), reduced difference from the reanalysis data around Siberia and Canada in spring (Fig. 9d). But the temperature rising around the North Pole in spring is still earlier. Temperature is slightly lower in North America, and higher in Sahara throughout all seasons. Since the topography of the model is not strictly identical to that of the reanalysis model, it is inevitable that the simulated sur-

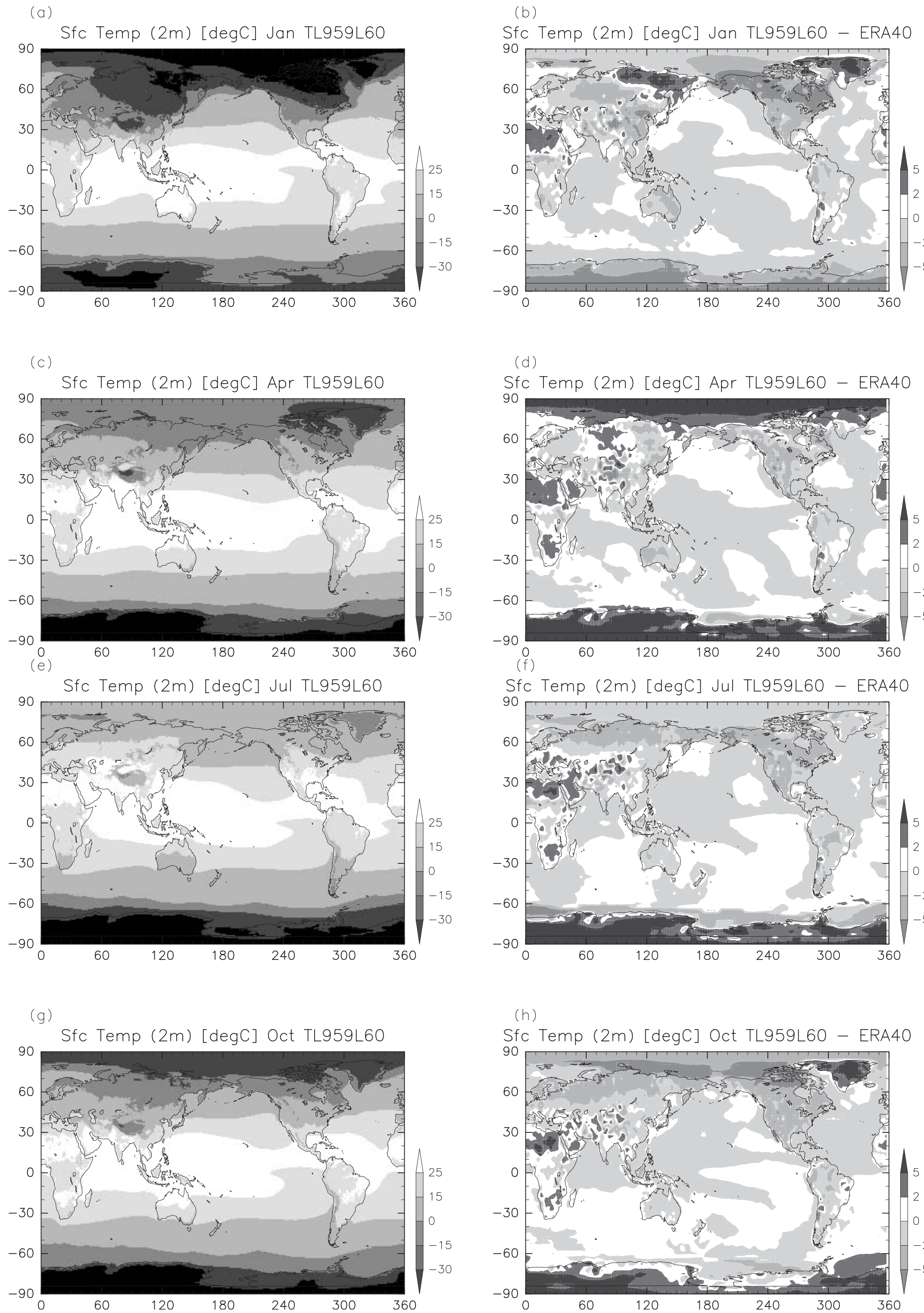

Fig. 9. Monthly mean surface air temperatures in °C in January (a, b), April (c, d), July (e, f), and October (g, h). (left) for the TL959 model, (right) difference from ERA40.

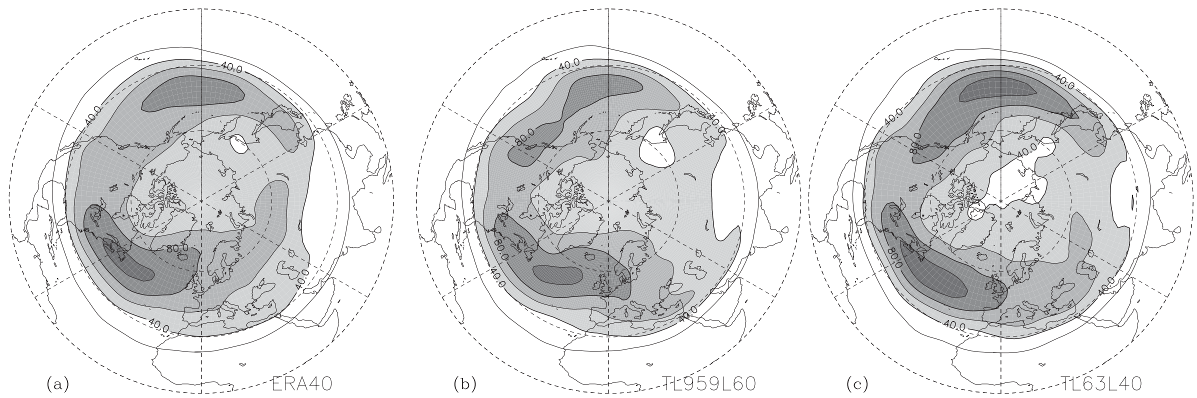

Fig. 10. Standard deviation of 2.5–6 days band-pass filtered geopotential height at 300 hPa in meter units in the boreal winter (from December to February) for (a) ERA40, (b) the TL959 model and (c) the TL63 model. Contour intervals are 20 m.

face temperatures differ from the reanalysis data associated with the difference of elevation, especially in mountain regions.

4.7 *Storm tracks*

Standard deviation of 2.5–6 days band-pass filtered geopotential height at 300 hPa is used as an index of the storm tracks. Figure 10 shows the result of the northern hemisphere in DJF for ERA40, the TL959 model and the TL63 model. We used the geopotential height data of the TL959 model averaged on every 1-degree grid due to the limitation of total data amount. The result is not dependent of the data resolution. The TL959 model well simulates the strength and peak positions of the storm tracks on the Pacific and the Atlantic. Extension to the downstream is slightly stronger in the eastern Pacific, and weaker in eastern Europe. Precipitations on the storm tracks are also well simulated, both on the Pacific and the Atlantic as long as the seasonal mean is concerned (Fig. 1). The TL63 model can also simulate storm tracks reasonably well, but the strength is larger, and the position of the Atlantic storm tracks is slightly more on the equatorial side, compared with the reanalysis data.

4.8 *Asian summer monsoon*

Hereafter, the model's performance of representing regional-scale phenomena is assessed. Figure 11 displays distributions of precipitation over Asia during summer (JJA), showing observational estimates by the Tropical Rainfall Measuring Mission (TRMM) 3B43 products, the results of the TL63, TL159 and TL959 models. Details of the TRMM and the instruments can be found in Kummerow et al. (2000). Regions of heavy precipitation on the west coast of India, east part of the Bay of Bengal, around the Philippines, southern part of Indochina, from middle China to Japan, are roughly simulated, even in the TL63 model. As the resolution increases up to TL959, the geographical distribution is improved, especially in the northern part of India, Taiwan and the south coast of Japan. Precipitation patterns following the mountains with the scale of about 100 km become resolved. In addition, representation of the locations of heavy precipitation over mountainous regions are much improved. It is clearly seen especially around 30°N 100°E, which is consistent with Kobayashi and Sugi (2004) in that the false precipitation around the area gradually decreases with increasing resolution. Some differences from the observation, however, still remain, even in the TL959 model. The rainfall amount on the west coast of India is over-estimated, and that around the south coast of China is under-estimated.

4.9 *Japan area*

Introduction of smaller-scale topography in the high-resolution simulation makes it possible to simulate realistic precipitation patterns, with the scale of less than 100 km, and to compare them with in-situ observations. Figure 12

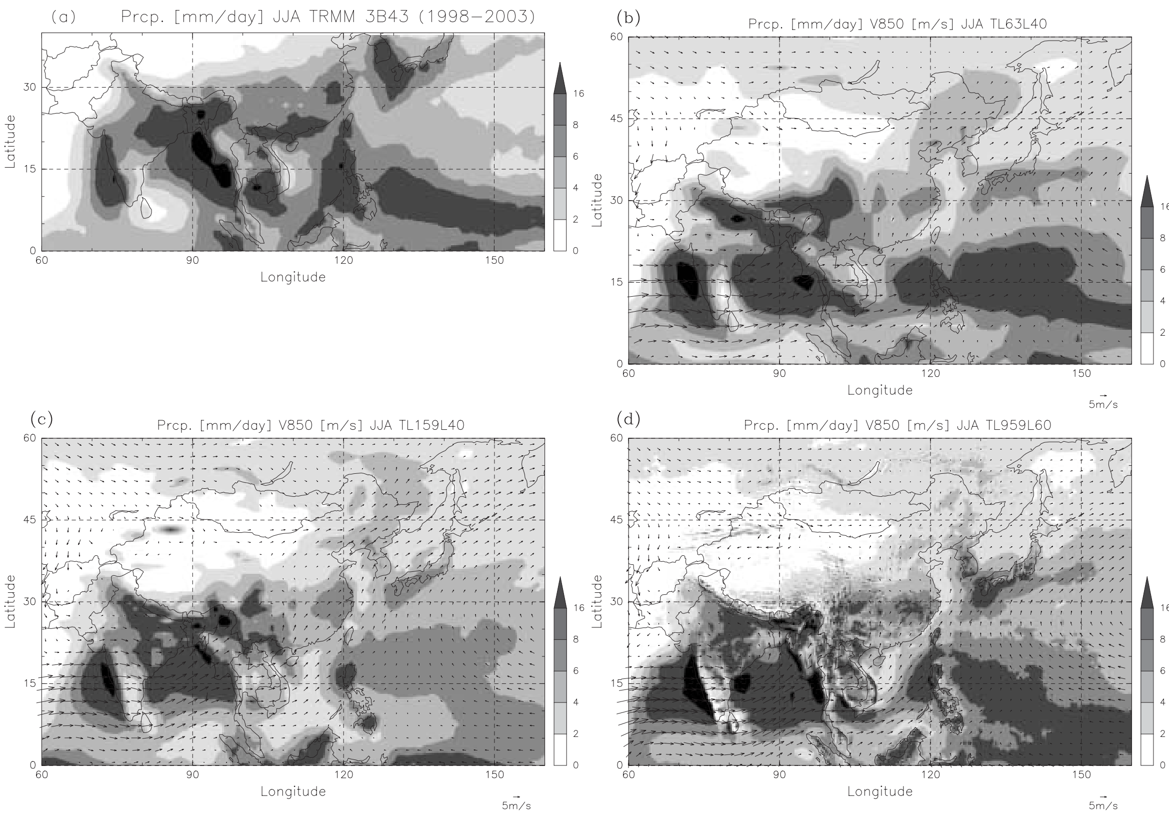

Fig. 11. Seasonal mean precipitation over Asian monsoon region in units of mm/day in JJA, for (a) the average from 1998 to 2002 estimated from TRMM 3B43, (b) for the TL63 model, (c) for the TL159 model, and (d) for the TL959 model. Note that TRMM 3B43 dataset covers only the equatorial side of 40 degrees north/south. Vectors in (b), (c), and (d) shows seasonal mean wind velocity at 850 hPa.

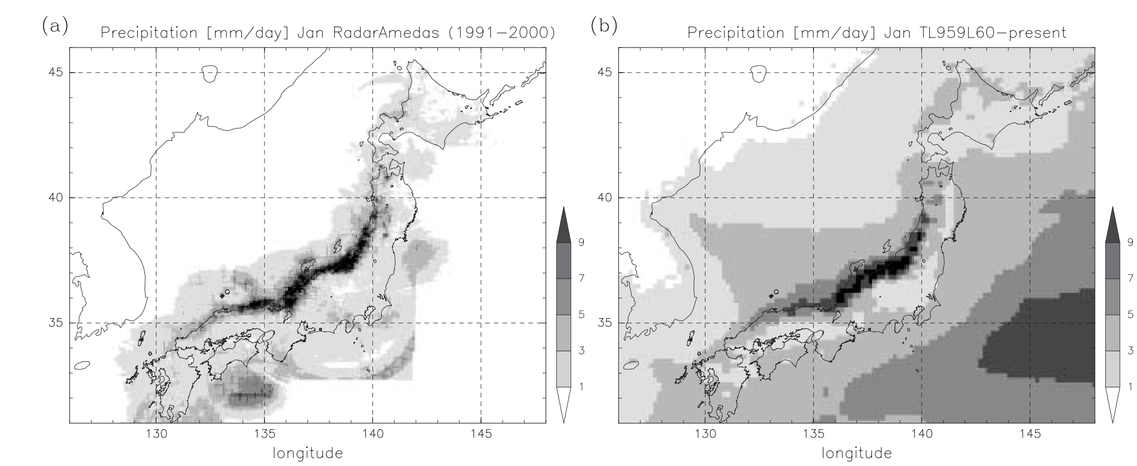

Fig. 12. Monthly mean precipitation over Japan in January. (a) 10-year-average from 1991 to 2000 for Radar-AMeDAS analysis, (b) 10-year-average for the TL959 model.

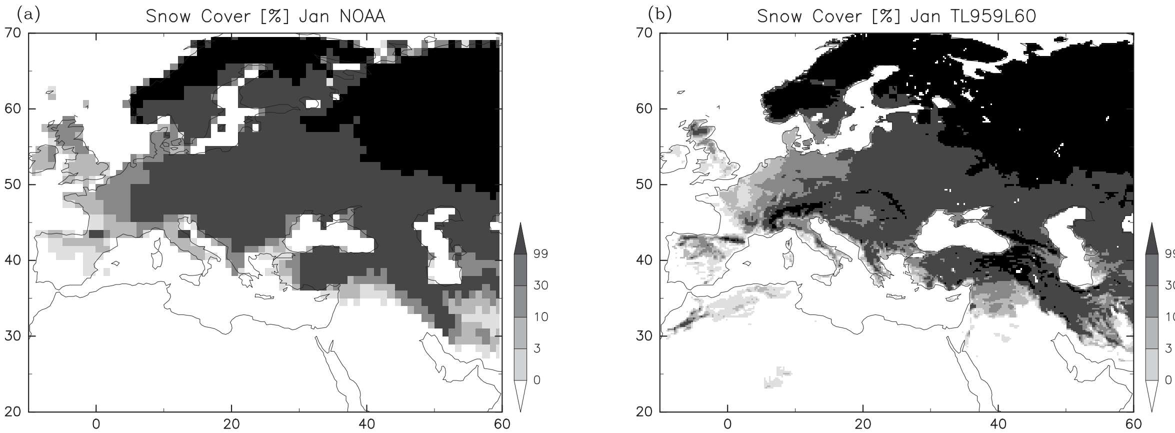

Fig. 13. Snow cover over European region in January in units of %. (a) for the climatological estimates by NOAA (averaged from 1971 to 1995), (b) for the TL959 model.

shows monthly mean precipitation around the Japan area in January. Figure 12a is an estimation of the radar-AMeDAS precipitation analysis averaged for 10 years. The radar-AMeDAS precipitation analysis is a dataset covering the Japan Islands and its coastal regions. It is estimated from observations of radars calibrated using densely distributed (about 17-km mesh) rain gauges. The calibration algorithm is described in Makihara (1996). The spatial resolution is approximately 5 km. In winter, a large amount of snow is observed on the northwest coast of Japan, due to steady winter monsoon northwesterlies from the Eurasian continent blocked by the topography of the Japan Islands. The results of the TL959 model presented in Fig. 12b show the model can simulate such detailed distributions of precipitation on the northwest coast of Japan.

4.10 Snow cover in Europe

Snow cover around Europe in January is compared with the observational data in Fig. 13. The snow-cover dataset is provided by the NOAA-CIRES Climate Diagnostics Center, Boulder, Colorado, USA, from their website at http://www.cdc.noaa.gov/. Spatial pattern, with a scale of several hundreds of kilometers, is well simulated in the model, such as 100% snow cover over Russia east of Moscow, and the northern half of Scandinavia, and more than 30% snow cover from east Europe to Turkey and the Aral Sea. Fine structure of snow cover over mountainous regions in the Alps, Pyrenees, and Kavkaz are also represented in the model. More detailed discussion is found in Hosaka et al. (2005).

5. Concluding remarks

We have developed a 20-km-mesh global atmospheric climate model. This model improves the representation of regional-scale climate by increasing horizontal resolution, due to better representation of topographical effects. At the same time, the quality of simulating climate in the global scale is kept in a large number of aspects, and moreover, some improvements in simulating climate are seen in horizontal distributions of seasonal precipitation (Figs. 1 and 2), zonal-mean zonal wind (Fig. 6), and wintertime storm tracks (Fig. 10). In order to achieve this at the unprecedentedly high resolution, some adjustments of physical parameterization were needed since the original model has been tuned carefully at coarse resolutions.

The most remarkable characteristic dependent on resolution is the increase of precipitation, especially that by grid-scale condensation (Fig. 3). This is consistent with the enhanced latent heat transport (Table 1) and warm bias in the tropical upper troposphere (Fig. 7). At the same time cloud amount in the lower and upper troposphere decreases (Fig. 4). These are basically seen also in other climate model studies (e.g., Kiehl and Williamson 1991), although sub-grid scale parameterizations are different with each other.

The model's performance of simulating the Indian and East Asian summer monsoons improves with finer resolution, consistent with previous studies (Tibaldi et al. 1990; Sperber et al. 1994; Stephenson et al. 1998; Kobayashi and Sugi 2004). Improvement is found not only in the locations of precipitation, but also in quantitative aspect. Details about this issue are not presented here but can be found in Kusunoki et al. (2005).

This paper is intended to demonstrate a capability of simulating large-scale, seasonal-mean climate state, even in such a high-resolution model. The model thus enables us to study global characteristics of small-scale phenomena and extreme events. It is also possible to focus on regions where regional climate models could not cover. A number of analyses on the small-scale issues have been, or are planned to be, reported in separate publications, including tropical cyclones (Oouchi et al. 2005), Baiu fronts (Kusunoki et al. 2005), indices of extreme events (Kamiguchi et al. 2005; Mizuta et al. 2005), and diurnal cycles of precipitation (Arakawa et al. 2005). These phenomena have been found to be simulated well in this model. Note that the treatment of sea ice has room for improvement, since a more sophisticated scheme used in the previous climate model of MRI has not been implemented in the present model. Therefore, care must be taken when one interprets the simulated results relevant to sea ice.

We have already performed four sets of climate simulations of over 10 years, using the 20-km-mesh model: 1) a present-day climate simulation using the observed climatological sea surface temperature (SST) as boundary conditions (10 years), 2) a global warming simulation forced by climatological SST plus anomalies around the year 2090 obtained from atmosphere-ocean coupled model simulations (10 years), 3) a present-day climate simulation (1979–1998) forced by the SST from a coupled model simulation (20 years), and 4) a global warming simulation (2080–2099) forced by the SST from a coupled model simulation (20 years). In this paper, only the results about the mean climate states of 1) were presented to examine fundamental performance of simulating the present-day climate. The results comparing these experiments for projection of global warming are also reported in the publications mentioned above. At the same time, simulations with a nonhydrostatic regional climate model have been performed (Yoshizaki et al. 2005; Yasunaga et al. 2005), of which lateral boundary conditions are provided by the calculations of this paper. They focus on East Asian summer monsoon, with horizontal grid size of 5 km.

The resolution used in the present model is almost the highest limit at which the parameterizations including cumulus convective schemes work in expected manner as in the coarser-resolution models. Based on a theoretical inference, hydrostatic approximation seems to be valid in this horizontal resolution, but may be violated in the higher-resolution model. At that stage, nonhydrostatic cloud-resolving global model will be necessary.

Acknowledgments

This work is a part of the "Kyosei Project 4: Development of Super High Resolution Global and Regional Climate Models" supported by Ministry of Education, Culture, Sports, Science and Technology (MEXT). The developments and calculations were carried out by the Kyosei-4 global modeling group. The authors would like to thank Prof. A. Arakawa, Dr. T. Tokioka, Dr. K. Ninomiya and Dr. K. Masuda for comments on the earlier version of the high-resolution model, and Earth Simulator Center for providing computational environments. GFD-DENNOU Library are used for the drawings. The authors also thank two anonymous reviewers whose comments improved the manuscript.

References

Aoki, T., A. Hachikubo, and M. Hori, 2003: Effects of snow physical parameters on shortwave broadband albedos. *J. Geophys. Res.*, **108**(D19), 4616, doi:10.1029/2003JD003506.

Arakawa, A. and W.H. Schubert, 1974: Interaction of cumulus cloud ensemble with the large-scale environment. Part I. *J. Atmos. Sci.*, **31**, 674–701.

Arakawa, O. and A. Kitoh, 2005: Rainfall diurnal variation over the Indonesian Maritime Continent simulated by 20 km-mesh GCM. *SOLA*, **1**, 109–112.

Brankovic, C. and D. Gregory, 2001: Impact of horizontal resolution on seasonal integrations. *Climate Dyn.*, **18**, 123–143.

Duffy, P.B., B. Govindasamy, J.P. Iorio, J. Milovich, K.R. Sperber, K.E. Taylor, M.F. Wehner, and S.L. Thompson, 2003: High-resolution simulations of global climate, part 1: present climate. *Climate Dyn.*, **21**, 371–390.

Gravel, S. and A. Staniforth, 1994: A mass-conserving semi-Lagrangian scheme for the shallow water equations. *Mon. Wea. Rev.*, **122**, 243–248.

Gregory, D., R. Kershaw, and P.M. Innes, 1997: Parameterization of momentum transport by convection. II: Tests in single-column and general circulation models. *Quart. J. Roy. Meteor. Soc.*, **123**, 1153–1183.

Habata, S., K. Umezawa, M. Yokokawa, and S. Kitawaki, 2004: Hardware system of the Earth Simulator. *Parallel Computing*, **30**, 1287–1313.

Harrison, E.F., P. Minnis, B.R. Barkstrom, V. Ramanathan, R.D. Cess, and G.G. Gibson, 1990: Seasonal variation of cloud radiative forcing derived from the Earth Radiation Budget Experiment. *J. Geophys. Res.*, **95**, 18,687–18,703.

Hortal, M., 2002: The development and testing of a new two-time-level semi-Lagrangian scheme (SETTLS) in the ECMWF forecast model. *Quart. J. Roy. Meteor. Soc.*, **128**, 1671–1687.

Hosaka, M., D. Nohara, and A. Kitoh, 2005: Changes in snow cover and snow water equivalent due to global warming simulated by a 20 km-mesh global atmospheric model. *SOLA*, **1**, 93–96.

Huffman, G.J., R.F. Adler, P. Arkin, A. Chang, R. Ferraro, A. Gruber, J. Janowiak, A. McNab, and B. Schneider, 1997: The Global Precipitation Climatology Project (GPCP) combined precipitation data set. *Bull. Amer. Meteor. Soc.*, **78**, 5–20.

IPCC, 2001: *Climate Change 2001: The Scientific Basis*. J.T. Houghton et al. Eds., Cambridge University Press, UK, 881 pp.

Iwasaki, T., S. Yamada, and K. Tada, 1989: A parameterization scheme of orographic gravity wave drag with the different vertical partitioning, part 1: Impact on medium range forcast. *J. Meteor. Soc. Japan*, **67**, 11–41.

JMA, 2002: *Outline of the operational numerical weather prediction at the Japan Meteorological Agency* (Appendix to WMO numerical weather prediction progress report). Japan Meteorological Agency, 157pp. (available online at http://www.jma.go.jp/JMA_HP/jma/jma-eng/jma-center/nwp/outline-nwp/index.htm)

Kamiguchi, K., A. Kitoh, T. Uchiyama, R. Mizuta, and A. Noda, 2005: Changes in precipitation-based extremes indices due to global warming projected by a global 20-km-mesh atmospheric model. *SOLA*, *submitted*.

Kanamitsu, T., K. Tada, T. Kudo, N. Sato, and S. Isa, 1983: Description of the JMA operational spectral model. *J. Meteor. Soc. Japan*, **61**, 812–828.

Kawai, H., 2003: Impact of a cloud ice fall scheme based on an analytically integrated solution. *CAS/JSC WGNE Research Activities in Atmospheric and Ocean Modeling*, **33**, 4.11–4.12.

———, 2004: Impact of a parameterization for subtropical marine stratocumulus. *CAS/JSC WGNE Research Activities in Atmospheric and Ocean Modeling*, **34**, 4.13–4.14.

———, 2005: Improvement of a cloud ice fall scheme in GCM. *CAS/JSC WGNE Research Activities in Atmospheric and Ocean Modeling*, **35**, 4.11–4.12.

Kiehl, J.T. and K.E. Trenberth, 1997: Earth's annual global mean energy budget. *Bull. Amer. Meteor. Soc.*, **78**, 197–208.

——— and D.L. Williamson, 1991: Dependence of cloud amount on horizontal resolution in the National Center for Atmospheric Research Community Climate Model. *J. Geophys. Res.*, **96**, 10,955–10,980.

Kobayashi, C. and M. Sugi, 2004: Impact of horizontal resolution on the simulation of the Asian summer monsoon and tropical cyclones in the JMA global model. *Climate Dyn.*, **93**, 165–176.

Kusunoki, S., J. Yoshimura, H. Yoshimura, A. Noda, K. Oouchi, and R. Mizuta, 2005: Change of Baiu in global warming projection by an atmospheric general circulation model with 20-km grid size. *J. Meteor. Soc. Japan*. *submitted*.

Kummerow, C. and Coauthors, 2000: The status of the Tropical Rainfall Measuring Mission (TRMM) after two years in orbit. *J. Appl. Meteor.*, **39**, 1965–1982.

Makihara, Y., 1996: A method for improving radar estimates of precipitation by comparing data from radars and raingauges. *J. Meteor. Soc. Japan*, **74**, 459–480.

Mellor, G.L. and T. Yamada, 1974: A hierarchy of turbulence closure models for planetary boundary layers. *J. Atmos. Sci.*, **31**, 1791–1806.

Mizuta, R., T. Uchiyama, K. Kamiguchi, A. Kitoh, and A. Noda, 2005: Changes in extremes indices over Japan due to global warming projected by a global 20-km-mesh atmospheric model. *SOLA*, **1**, 153–156.

Moorthi, S. and M.J. Suarez, 1992: Relaxed Arakawa-Schubert: A parameterization of moist convection for general circulation models. *Mon. Wea. Rev.*, **120**, 978–1002.

Nakagawa, M. and A. Shimpo, 2004: Development of a cumulus parameterization scheme for the operational global model at JMA. *RSMC Tokyo-Typhoon Center Techninal Review*, **7**, 10–15.

Ohfuchi, W., H. Nakamura, M.K. Yoshioka, T. Enomoto, K. Takaya, X. Peng, S. Yamane, T. Nishimura, Y. Kurihara, and K. Ninomiya, 2004: 10-km mesh meso-scale resolving simulations of the global atmosphere on the Earth Simulator—preliminary outcomes of AFES (AGCM for the Earth Simulator)—, *J. Earth Simulator*, **1**, 8–34.

Oouchi, K., J. Yoshimura, H. Yoshimura, R. Mizuta, S. Kusunoki, and A. Noda, 2006: Tropical cyclone climatology in a global-warming climate as simulated in a 20 km-mesh global atmospheric model. *J. Meteor. Soc. Japan*, in press.

Pan, D.-M. and D. Randall, 1998: A cumulus parameterization with a prognostic closure. *Quart. J. Roy. Meteor. Soc.*, **124**, 949–981.

Phillips, T.J., L.C. Corsetti, and S.L. Grotch, 1995: The impact of horizontal resolution on moist processes in the ECMWF model. *Climate Dyn.*, **11**, 85–102.

Pope, V.D. and R.A. Stratton, 2002: The processes governing horizontal resolution sensitivity in a climate model. *Climate Dyn.*, **19**, 211–236.

Priestley, A., 1993: A quasi-conservative version of the semi-Lagrangian advection scheme. *Mon. Wea. Rev.*, **121**, 621–629.

Randall, D. and D.-M. Pan, 1993: Implementation of the Arakawa-Schubert cumulus parameterization with a prognostic closure. Meteorological Monograph/*The representation of cumulus convection in numerical models*, **46**, 145–150.

Reynolds, R.W. and T.M. Smith, 1994: Improved global sea surface temperature analysis using optimum interpolation. *J. Climate.*, **7**, 929–948.

Ritchie, H., C. Temperton, A. Simmons, M. Hortal, T. Davies, D. Dent, and M. Hamrud, 1995: Implementation of the semi-Lagrangian method in a high-resolution version of the ECMWF forecast model. *Mon. Wea. Rev.*, **123**, 489–514.

Sellers, P.J., Y. Mints, Y.C. Sud, and A. Dalcher, 1986: A simple biosphere model (SiB) for use within general circulation models. *J. Atmos. Sci.*, **43**, 505–531.

Shibata, K., H. Yoshimura, M. Ohizumi, M. Hosaka, and M. Sugi, 1999: A simulation of troposphere, stratosphere and mesosphere with an MRI/JMA98 GCM. *Pap. Meteor. Geophys.*, **50**, 15–53.

Simmons, A.J. and Gibson, J.K., 2000: *The ERA-40 Project Plan, ERA-40 Project Report Series 1*. ECMWF. Shinfield Park, Reading, UK, 63pp.

Slingo, J.M., 1987: The development and verification of a cloud prediction scheme in the ECMWF model. *Quart. J. Roy. Meteor. Soc.*, **113**, 899–927.

Smith, R.N.B., 1990: A scheme for predicting layer clouds and their water content in a general circulation model. *Quart. J. Roy. Meteor. Soc.*, **116**, 435–460.

Sommeria, G. and J.W. Deardorff, 1977: Subgrid-scale condensation in models of nonprecipitating clouds. *J. Atmos. Sci.*, **34**, 344–355.

Sperber, K.R., S. Hamed, G.L. Potter, and J.S. Boyle, 1994: Simulation of the northern summer monsoon in the ECMWF model: sensitivity to horizontal resolution. *Mon. Wea. Rev.*, **122**, 2461–2481.

Stephenson, D.B., F. Chauvi, and J.-F. Royer, 1998: Simulation of the Asian Summer Monsoon and its dependence on model horizontal resolution. *J. Meteor. Soc. Japan*, **76**, 237–265.

Stratton, R.A., 1999: A high resolution AMIP integration using the Hadley Centre model HadAM2b. *Climate Dyn.*, **15**, 9–28.

Sundqvist, H., 1978: A parameterization scheme for non-convective condensation including prediction of cloud water content. *Quart. J. Roy. Meteor. Soc.*, **104**, 677–690.

Tanaka, T.Y., Orito, K., Sekiyama, T., Shibata, K., Chiba, M., and Tanaka, H., 2003: MASINGAR, a global tropospheric aerosol chemical transport model coupled with MRI/JMA98 GCM: Model description. *Pap. Meteor. Geophys.*, **53**, 119–138.

Temperton, C., M. Hortal, and A.J. Simmons, 2001: A two-time-level semi-Lagrangian global spectral model. *Quart. J. Roy. Meteor. Soc.*, **127**, 111–127.

Tibaldi, S., T.N. Palmer, C. Brankovic, and U. Cubasch, 1990: Extended range predictions with ECMWF models: influence of horizontal resolution on systematic error and forecast skill. *Quart. J. Roy. Meteor. Soc.*, **116**, 835–866.

Williamson, D.L., J.T. Kiehl, and J.J. Hack, 1995: Climate sensitivity of the NCAR Community Climate model (CCM2) to horizontal resolution. *Climate Dyn.*, **11**, 377–397.

Wu, X. and M. Yanai, 1994: Effects of vertical wind shear on the cumulus transport of momentum: Observations and parameterization. *J. Atmos. Sci.*, **51**, 1640–1660.

Xie, P. and P.A. Arkin, 1997: Global precipitation: a 17-year monthly analysis based on gauge observations, satellite estimates, and numerical model outputs. *Bull. Amer. Meteor. Soc.*, **78**, 2539–2558.

Yasunaga, K., M. Yoshizaki, Y. Wakazuki, C. Muroi, K. Kurihara, A. Hashimoto, S. Kanada, T.

Kato, S. Kusunoki, K. Oouchi, H. Yoshimura, R. Mizuta, and A. Noda, 2006: Changes in the Baiu frontal activity in the global warming climate simulated by super-high-resolution global and cloud-resolving regional models. *J. Meteor. Soc. Japan*, **84**, 199–220.

Yoshimura, H. and T. Matsumura, 2003: A semi-Lagrangian scheme conservative in the vertical direction. CAS/JSC WGNE *Research Activities in Atmospheric and Ocean Modeling*, **33**, 3.19–3.20.

——— and T. Matsumura, 2005: A two-time-level vertically-conservative semi-Lagrangian semi-implicit double Fourier series AGCM. CAS/JSC WGNE *Research Activities in Atmospheric and Ocean Modeling*, **35**, 3.27–3.28.

Yoshizaki, M., C. Muroi, S. Kanada, Y. Wakazuki, K. Yasunaga, A. Hashimoto, T. Kato, K. Kurihara, A. Noda, and S. Kusunoki, 2005: Changes of Baiu (Mei-yu) frontal activity in the global warming climate simulated by a non-hydrostatic regional model. *SOLA*, **1**, 25–28.